Available online at www.sciencedirect.com

SCIENCE DIRECT

Journal of the European Ceramic Society 25 (2005) 1225–1239

www.elsevier.com/locate/jeurceramsoc

Creep of directionally solidified alumina/YAG eutectic monofilaments

L.E. Matson[a,*], N. Hecht[b]

[a] Materials and Manufacturing Directorate, Air Force Research Laboratory, USAF/AFRL/MLLN, WPAFB, OH 45433, USA
[b] University of Dayton, Dayton, OH 45469, USA

Abstract

Multi-phase—single crystal oxide fibers offer the best choice for reinforcing oxide matrix composites because they have superior creep resistance up to 1700 °C without significant strength loss at moderate temperatures due to growth of processing flaws. In this work, Directionally Solidified Al_2O_3–YAG eutectic fibers were grown at various rates by the Edge-defined, Film-fed Growth (EFG) method and their microstructure, microstructural stability and creep properties were studied. A methodology was developed in order to determine if the creep behavior of a fiber was affected by any heterogeneous coarsening defects. The creep behavior could be rationalized using a threshold stress concept with activation energy of 1100 kJ/mol K. TEM analysis of the crept fibers suggested that the Sapphire phase was deforming by a dislocation mechanism, while the YAG phase deformed by a diffusional mechanism. A creep model was developed which contained geometrical factors for describing the microstructure. Analysis of the data showed that the creep resistance would increase to single crystal values as the phase aspect ratio increased. Further, these two phases—single crystal structures exhibit a flaw-independent strength and are suggested to have a decrease in slow crack growth rate as the transverse phase size decreases.

Keywords: Directionally solidified Al_2O_3–YAG eutectics; Fibers; Microstructure-final; Strength; Creep

1. Introduction

Oxide/oxide composites are being considered for long-term high temperature operations in an air environment. These composites require thermal-chemical compatibility with their use environment as well as thermal-mechanical compatibility with each other.[1–4] One of the most favorable couple is alumina (Al_2O_3) with yttrium–aluminum–garnet (YAG) ($Y_3Al_5O_{12}$). Unfortunately, polycrystalline fibers of aluminum oxide (α-Al_2O_3)[5–9] and YAG[10–13] are limited to a maximum useful temperature of between 1000 and 1200 °C by fiber strength degradation and by creep. Rapid strength loss is attributed to grain growth while high creep rates are attributed to diffusional creep mechanisms; both phenomena are a consequence of the presence of grain boundaries.

Single phase-single crystal fibers show superior creep resistance compared to polycrystalline fibers, because of the elimination of grain boundaries, which forces deformation to occur in the bulk by dislocation mechanism rather than interface diffusion controlled.[14–26] Most single crystal work has focused on sapphire (single crystal alumina), which has a highly anisotropy rhombohedral crystal structure. This structure results in a large variability in creep resistance with orientation.[14–16] The actual use temperature of a composite containing sapphire fiber may be as low as 1200 °C where basal slip limits the creep behavior. A better candidate for a creep resistant single phase-single crystal fiber is yttrium-aluminum-garnet. It has a complex cubic crystal structure; therefore, a more isotropic creep behavior. Additionally, YAG has a large unit cell, which makes dislocation generation and mobility difficult. General Electric Inc. and MSNW Inc. showed very good creep behavior for several orientations of single crystal YAG up to 1700 °C.[17–21] Unfortunately, they also showed that single crystal fibers are limited by a low fracture toughness (K_c) and strength degradation at moderate temperatures caused by flaws that undergo slow crack growth.[22–32]

In hopes of overcoming the shortcomings of both polycrystalline and single crystal fibers, two-phase single crystals structures (Directionally Solidified Eutectics [DSE]) have been explored because they should provide better strength, creep resistance, and toughness. The hypothesis here is that

---

* Corresponding author. Tel.: +1 937 255 9842; fax: +1 937 656 4296.

0955-2219/$ – see front matter © 2005 Elsevier Ltd. All rights reserved.
doi:10.1016/j.jeurceramsoc.2005.01.005

the tensile strength and toughness of a eutectic fiber may be increased due to the presence of a large number of interphase boundaries across the fiber cross-section (i.e., a fine transverse phase spacing). This strengthening phenomenon is similar to that observed in polycrystalline ceramic materials where strength is inversely proportional to the square root of the grain size (a Hall-Petch type relationship). In eutectics this strengthening is believed to occur due to inherent processing flaws being constrained within the phase spacing during solidification. Enhanced creep resistance should be realized when the phases have high aspect ratio's and are well aligned with the fiber growth axis (tensile axis). This will increase both the diffusion path lengths, as well as provide a larger dislocation glide and climb barrier, both limiting the creep behavior.

2. Background

Directionally Solidified Alumina/YAG eutectic [DS-AYE] have been fabricated into bulk rods and monofilaments using single crystal melt processes of Edge-defined Film-fed Growth (EFG)[33–43] and Laser Heated Float Zoning (LHFZ).[43–46] The bulk eutectic showed slightly better K_c values than its single crystal constituents, but its creep resistance was limited by deformation and decohesion at misaligned colony/cell boundaries and its tensile strength was low due to the large phase size.[38,39] EFG growth experiment on small rods and monofilaments conducted at UES, Inc.[41] and Saphikon, Inc.[42,43] showed the following results:

1. A uniform thermal gradient eliminates the growth of colony/cell boundaries.
2. Pull rate was the dominant processing parameter for increasing the steepness of the thermal gradient during solidification, hence reducing the microstructural scale in the transverse section. Reducing the fiber diameter showed only a minimal effect.
3. The room temperature fast fracture strength is proportional to the inverse square of the transverse phase size (a Hall-Petch type relationship).
4. Phase alignment and aspect ratio appeared to have increased in some areas of the fiber when the pull rate was increased.
5. A transition from coarser script type morphology to an aligned finer rod structure was observed at extremely high pull rates and these fibers showed the highest tensile strength.

Strength retention in polycrystalline material is usually governed by homogeneous coarsening or grain growth according to ($t^{1/2}$) type kinetics. However, in the two phase-single crystal case, the kinetics should be much slower according to Ardell[45–48] because volume or interphase diffusion should control the coarsening rates with either ($t^{1/3}$) or ($t^{1/4}$) kinetics. Yang[49–51] showed that in the DS-AYE material, homogeneous coarsening was in fact very slow and occurs at ($t^{1/4}$) kinetics presumably due to diffusion of yttrium ion (the largest and heaviest ion in the system). Unfortunately, in this system strength limiting defects were observed on the fiber surface as abnormal coarsened areas after long term anneals of fibers.[45–55] Initially, this was attributed to a discontinuous coarsening mechanism, which has been observed in some metallic eutectics.[56,57] These defects where analyzed in the TEM using EDX and found to be caused by a surface reaction between the fiber constituents and silicon containing dust and dirt from the air.[58] It is important to note that in a real composite where the fiber surface can be keep clean prior to coating and consolidation into a matrix; the fiber strength should be limited by homogeneous coarsening and not these extrinsic defects.

Compression creep studies on bulk DS-AYE composites[54,55,59,60] showed that the creep resistance of the material was much better than polycrystalline alumina or alumina/YAG mixture.[8–13,61,62] The creep stress exponent was on the order of five irrespective of the temperature. This suggests a power law creep mechanism operating without generating a backstress. TEM analysis showed some dislocation generation occurred in the single crystal alumina phase, but little dislocation activity was found in the single crystal YAG phase. Compression creep strength was higher than the polycrystalline mixtures and rupture occurred by decohesion at the high angle grain boundaries, if present, or on the low angle cell/colony boundaries. In either case, it was envisioned that this situation would be detrimental to tensile creep. A creep model[60] was proposed that suggested that if grain and colony free material could be fabricated and high aspect ratio phases developed that was well aligned with respect to the tensile loading axis, then tensile creep resistance and strength could be increased substantially. It was envisioned that very thin DS-AYE fibers could possibility meet these requirements.

3. Experiment procedures

3.1. Fiber processing

DS-AYE monofilaments [diameter = 127 μm] were produced by UES Inc., of Dayton, OH[40,41,55] using the EFG method. Fibers were pulled at a temperature of ≅1910 °C from two tips on the die set and extraction rates of 0.1, 0.25, and 0.5 in./min. Tip 1 was at the center of the EFG die and tip 4 was along the edge next to the furnace elements. Irregular spaced, degenerative microstructures referred to as "script type" morphology was produced within this stable growth field (Fig. 1a–d). The faster the pull rate the fine the transverse microstructure and the stronger the fiber. Fibers pulled at faster rates (up to 0.9 in./min) produce a dual microstructure consisting of very fine script type morphology with patches of even finer regular rod shaped eutectic scattered throughout. These were the strongest fibers with RT

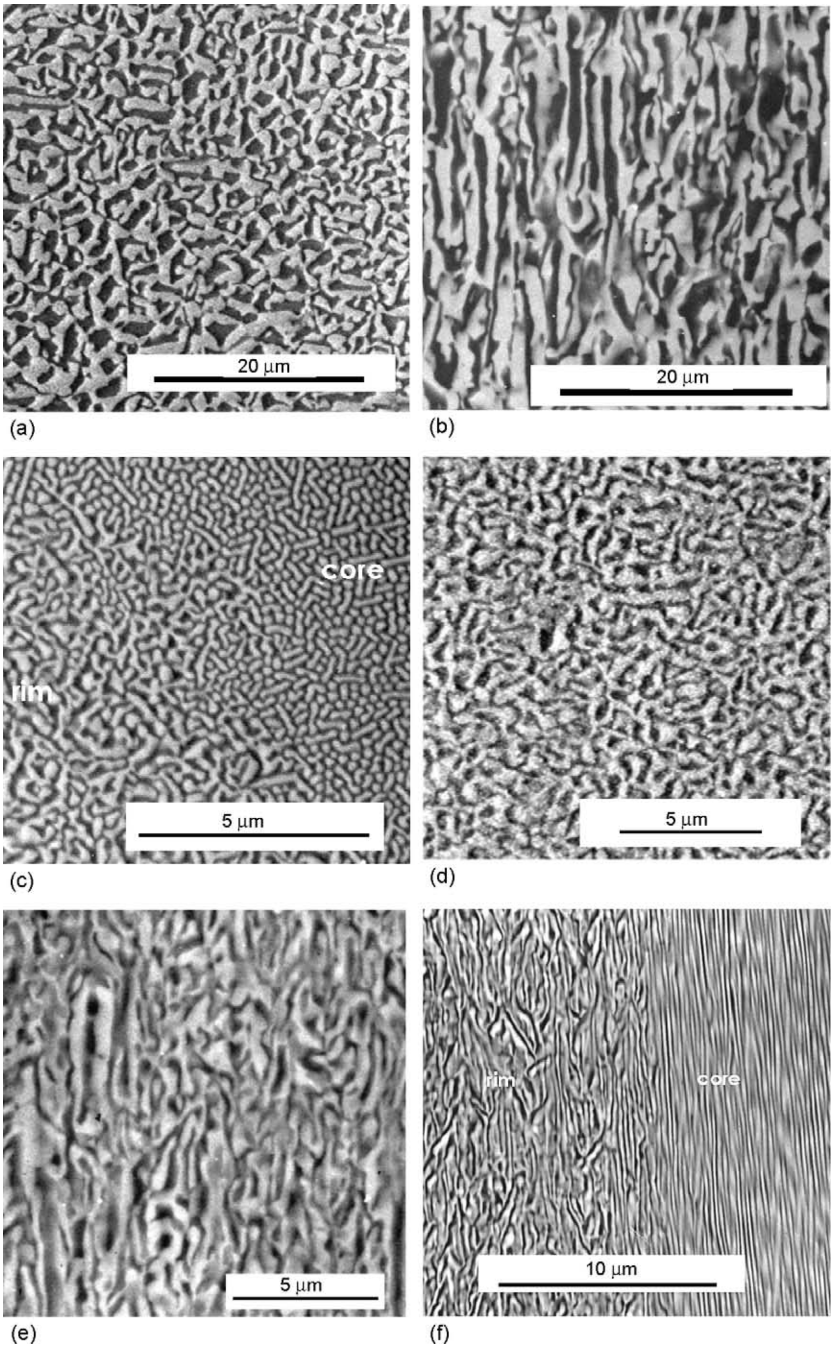

Fig. 1. SEM backscatter micrographs of AYE monofilaments from two vendors. Transverse (a) and longitudinal (b) cross-sections of the uniform script morphology grown by UES at 0.1 in./min from tip 1. Transverse (c) and longitudinal (d) cross-sections of the uniform script morphology grown by UES at 0.5 in./min from tip 1. Transverse (e) and longitudinal (f) cross-sections of the dual morphology grown by Saphikon at 1.0 in./min {referred to as SAP-133}. Note the fiber rim is script morphology while the fiber core is wavy rod morphology.

tensile strengths approaching 3 MPa. Unfortunately, continuous fiber growth was difficult to maintain at these pull rate so only a small quantity of fiber was produced not enough for creep testing.

DS-AYE monofilaments [diameter = 133 μm] were also produced by Saphikon, Inc., Milford, NH.[42,43] Results from their program were similar to that of the UES program except for one growth run conducted at a very fast rate of 1.0 in./min [Saphikon designation YAE-1, machine 28, die 29]. As expected this monofilament contained a dual morphology. However, here the very fine irregular spaced script morphology was formed at the rim of the fiber (thickness ≅ 0.30 μm) and an even finer rod structure at the core (Fig. 1e and f).The rod morphology occupied approximately 50 vol.% of the fiber and tended to run parallel to the growth axis but meander somewhat around the center of the fiber. This fiber is referred to as SAP-133 in the stability study[58] and here in the creep study. This fiber had a RT tensile strength of 2.4 GPa (347 ksi) with a standard deviation of ±0.33 GPa (48 ksi).

3.2. *Microstructural characterization*

Scanning Electron Microscopy (SEM) micrographs of the as-produced, annealed, and crept fibers were obtained from the surfaces, transverse cross-sections, and longitudinal cross-sections at various magnifications in both the secondary electron (SEI) and back scattered electron (BEI) imaging modes on a (Leica 360 FEG-SEM). The chemistry of each phase was obtained in the SEM by using Energy Dispersive X-ray Spectrometer (EDS) (Noran Inc., model 219B-1SPS). The backscattered electron SEM micrographs of the transverse and longitudinal cross-sections for each fiber were digitally scanned and analyzed for phase size, shape, and distribution using the National Institute of Health shareware called "NIH Image".

Transmission Electron Microscopy (TEM) studies were also conducted on thin foil samples prepared for each condition. Thin foils were fabricated by tripod polishing and argon gas ion milled to perforation. These TEM thin foils were carbon coated for conductivity and characterized in a Transmission Electron Microscope (Philips CM 200 keV FEG-TEM). Bright field (BF), dark field (DF), and selected area diffraction (SAD) analysis were used to observe the microstructural features in the thinned area. TEM also allowed for determination of the crystallographic orientation relationships between phases. Digital Parallel Electron Energy Loss spectrometry and Energy Dispersive X-ray was used to study the phase chemistry.

3.3. *Creep testing*

A cold grip-constant load tensile creep rig was designed and built to operate in a room air environment up to 1700 °C. Details of the design are given by Sheehan.[21,25,26,63,64] A sapphire tube furnace was radiation heated by an inductively coupled molybdenum suscepter. Argon was used to protect the molybdenum susceptor, which resided between the o.d. of a 1/8-in. diameter sapphire tube and the i.d. of a 2-in. diameter quartz tube. Each tube was approximately 8 in. long. An atmosphere of room air was maintained around the monofilament in the i.d. of the sapphire tube. The furnace temperature was controlled by a thermocouple placed between the sapphire tube and the molybdenum susceptor. Furnace profiling was done by lowering an optical thermocouple down the interior of the sapphire tube. Profiling was conducted prior to and after each creep test to assure no temperature transits occurred during testing. The thermal profiles were used in an integration scheme to determine the effective gage length at 1400, 1500, 1600, and 1700 °C.[65] Displacements were measured by attaching a linear variable displacement transducer (Lucas Schaevitz model #050 DC-E) with the core-rod attached between the end of the fiber and a basket containing weights. The displacement during heat up and creep was recorded on a continuous spooled chart recorder with a resolution of 0.0005-in. displacement per division on the chart paper. Constant load creep tests were terminated upon rupture or after ≅200 h of exposure. Over 100 creep tests were performed at loads from 100 to 500 MPa and temperatures from 1400 to 1700 °C.

The displacement versus time creep data was converted to incremental strain rate versus strain data. This analysis was conducted as a screen test to assure that the creep behavior went through a minimum creep rate stage prior to failure. If it did the experiment was then considered valid for steady state creep analysis, if it did not, the experiment was considered invalid and not used in the analysis. The monofilaments from the creep test considered invalid for steady state analysis were still characterized to see if premature failure in the primary creep stage was caused by the growth of heterogeneous coarsening defects within the gage length.[67] In about half of the creep test conducted in this study, rupture initiates at these coarsening sites while the fibers were still in the primary creep regime.

4. Results and discussions

4.1. *Microstructural analysis*

Backscattered electron SEM micrographs of the transverse and longitudinal cross-sections were taken of each fiber along with their associated Fast Fourier Transformation image (FFT). Select fibers are shown in (Fig. 1a–f). In these images the single crystal YAG phase appears bright and is distributed in a matrix of single crystal alumina (the dark phase). The FFT of each image contains information about the size, shape, and distribution of the phases in the microstructure. A threshold FFT was generated and the ratio of its major to minor axis provided a dimensionless parameter used here to quantify the degree of alignment in the microstructure. All of the longitudinal cross-sections showed an elliptical shaped FFT because their microstructures were aligned with the growth axis. All transverse cross-sections showed spherical shaped FFTs implying a uniform distribution of phases. Phase size cannot be determined using the FFTs therefore a digital phase size analysis program was written in NIH Image to quantify the microstructure on pixel-by-pixel bases.

The average phase dimensions and their standard deviations for the transverse cross-sections (TCS), the longitudinal cross-section in the thickness direction (LCS-T), and the longitudinal cross-section in the length direction (LCS-L) are provided in Table 1. Note, the (LCS-L) is not a measure of the YAG phase continuity but the frequency of the phase migration off the growth axis caused by out-of-plane growth micro-faults that result in branching. This average phase length between faults (LCS-L) and the average phase thickness (TCS) becomes important in explaining the creep behavior as will be discussed in a latter section.

Table 1
Summary of the microstructural analysis

Vendor	Growth rate (in./min)	Tip #	Average diameter (µm)	Morphology	Analysis direction	Average YAG (white) (µm)	Average alumina (Bk) (µm)	Volume fraction % YAG	FFT ratio	FF σ (ksi)	YAG TCS LCS-L	YAG LCS-T TCS	Creep geometrical factor
UES	0.1	1	130 ± 2	TCS	TCS	0.8965	0.75415	58 ± 2	1.034	124	R_1	R_2	4.94
				Chinese script	Width	+0.7574	+0.6357				0.4572	1.13	
				Sharp facets		−0.4046	−0.3452						
					LCS-T	1.01997	0.7290	60 ± 2	2.55				
						+0.8528	+0.5385						
						−0.4646	−0.3975						
				LCS	LCS-L	1.9615	1.3814	60 ± 2	2.55				
				Good alignment	Length	+2.5885	+1.7480						
						−0.7716	−0.7716						
UES	0.1	4	133 ± 2	TCS	TCS	0.96015	0.72119	58 ± 2	1.019	120	R_1	R_2	4.13
				Chinese script	Width	+0.8251	+0.5322				0.4466	1.327	
				Sharp facets		−0.4443	−0.1946						
					LCS-T	1.2746	1.0076	60 ± 2	2.3575				
						+0.9507	+0.5931						
						−0.5445	−0.3733						
				LCS	LCS-L	2.150	1.5694	60 ± 2	2.3575				
				Good alignment	Length	+2.363	+1.4692						
				Sharp facets		−1.126	−0.7589						
UES	0.25	1	131 ± 2	TCS	TCS	0.6939	0.51637	60 ± 2	1.005	137	R_1	R_2	14.06
				Chinese script	Width	+0.4833	+0.2774				0.6199	0.98	
				Sharp facets		−0.2850	−0.1805						
					LCS-T	0.6807	0.5327	59 ± 2	2.3884				
						+0.4760	+0.3021						
						−0.2801	−0.2801						
				LCS	LCS-L	1.1192	0.8419	59 ± 2	2.3884				
				Good alignment	Length	+1.3208	+1.7267						
				Sharp facets		−0.0839	−0.4105						
UES	0.25	4	130 ± 2	TCS	TCS	0.5353	0.3399	58 ± 2	1.00	142	R_1	R_2	23.87
				Chinese script	Width	+0.5212	+0.3679				0.625	1.11	
				Sharp facets		−0.2640	−0.1916						
					LCS-T	0.5947	0.4511	58 ± 2	2.02				
						+0.5585	+0.3907						
						−0.2880	−0.2094						
				LCS	LCS-L	0.8580	0.6443	58 ± 2	2.02				
				Good alignment	Length	+1.2453	+0.8358						
				Sharp facets		−0.5080	−0.3638						
UES	0.5	1	125 ± 2	TCS	TCS	0.3316	0.2490	58 ± 2	1.01	217	R_1	R_2	58
				Chinese script	Width	+0.2747	+0.1779				0.5988	1.05	
				Rounded facets		−0.1502	−0.0983						
					LCS-T	0.3312	0.2518	60 ± 2	2.00				
						+0.2648	+0.1610						
						−0.1509	−0.0983						
				LCS	LCS-L	0.5539	0.3955	60 ± 2	2.55				
				Some aligned	Length	+0.6640	+0.4086						
				Wavy facets		−0.3020	−0.2007						

Table 1 (*Continued*)

Vendor	Growth rate (in./min)	Tip #	Average diameter (μm)	Morphology	Analysis direction	Average YAG (white) (μm)	Average alumina (Bk) (μm)	Volume fraction % YAG	FFT ratio	FF σ (ksi)	YAG TCS LCS-L	YAG LCS-T TCS	Creep geometrical factor
UES	0.5	4	128 ± 2	TCS	TCS	0.4017	0.2943	59 ± 2	1.01	201	R_1	R_2	35
				Chinese script	Width	+0.2944	+0.2010				0.5649	1.27	
				Rounded facets		−0.1199	−0.1194						
					LCS-T	0.5101	0.4013	59 ± 2	1.51				
						+0.3157	+0.1778						
						−0.1951	−0.1213						
				LCS	LCS-L	0.7164	0.5601	59 ± 2	1.51				
				Good alignment	Length	+0.6540	+0.4216						
				Sharp facets		−0.3419	−0.2406						
SAP-133	<1.0	N/A	133 ± 3	TCS	TCS	0.2374	0.1676	58 ± 2	1.00	320	R_1	R_2	76
(Rim)				Chinese script	Width	+0.1352	+0.1043				0.4785	0.99	
				Very rounded facets		−0.1056	−0.643						
					LCS-T	0.2362	0.1911	59 ± 2	2.02				
						+0.1346	+0.0812						
						−0.857	−0.0570						
				LCS	LCS-L	0.4951	0.3819	59 ± 2	2.02				
				Good alignment	Length	+0.5036	+0.3187						
				Very wavy facets		−0.2496	−0.1737						
SAP-133	N/A	N/A	133	TCS	TCS	0.1681	0.1235	59 ± 2	1.00	3.23	3.42	1.04	2
(Core #3)				Rod/plate	W	+0.0760	+0.0859				R_1	R_2	
Wavy				Few facets		−0.0524	−0.0501				0.2924		
					LCS-T	0.1744	0.1391	60 ± 2	3.3 to 0.29				
						+0.0593	+0.0219						
						−0.0443	−0.0189						
				LCS	LCS-L	0.5752	0.4861	60 ± 2	3.3 to 29				
				Wavy align	L	+1.1864	+0.0912						
				Meandering		−0.3874	−0.3171						
SAP-133				LCS	LCS-L	20	20	60 ± 2	N/A		R_1	R_2	0.05
Core													
Aligned				Good align	L						0.0056	1.080	

The following trends were found in the microstructural analysis:

(a) The faster the pull rate, the finer the average TCS phase size in the script and rod microstructures. This follows from the Jackson and Hunt formula.[66,67]
(b) The faster the pull rate, the finer the LCS-L fault spacing in the irregularly spaced, script structures. This indicates the fault or branch site spacing decreases with an increase in pull rate. *Note this was not anticipated prior to this analysis.*
(c) The rod structure found in the core of the Saphikon 133 monofilament also had a very fine TCS phase size. However, it had a very large distance between growth faults or branches (LCS-L). *Note this is opposite that of the script morphology.* This microstructual feature should provide the best creep resistance according to the hypothesis.
(d) No recalescence (impingement of like phases) was observed in the transition region between the rod and script structure. This suggested that this morphology is not a colony/cell boundary but a change in the growth mode possibly caused by the growth velocity limiting the number of L-S micro-facet configurations on the YAG phase resulting in a lamella-rod transition with velocity as predicted by Croker.[68–71]
(e) The volume fraction of phases was determined digitally to be approximately 59% ±2 vol.% YAG for all the fibers. This is slightly higher then predicted by the binary phase diagram.[72–76]
(f) Qualitative chemical phase analysis on the as-received, annealed, and crept fibers using X-ray powder diffraction, EDX in the SEM, Selected Area Diffraction and Convergent Beam Electron Diffraction (CBED) in the TEM, suggested only alumina and YAG phases were present. No evidence that the YAP phase was present.
(g) Selected Area Diffraction analysis showed that all the fibers contained the same orientation relationship (OR) between phases (at least within a 3 degrees variation). The OR is described as $(0\,0\,0\,1)_A//(1\,1\,1)_Y$, $(1\,0\,\bar{1}\,0)_A/(0\,1\,\bar{1})_Y$, and $[1\,1\,\bar{2}\,0]_A/[2\,\bar{1}\,\bar{1}]_Y$. No habit plane was identified. It is important to note that this OR differs from that observed in the bulk eutectic which was $(0\,0\,0\,1)_A//(1\,1\,2)_Y$, $(2\,\bar{1}\,\bar{1}\,0)_A//(1\,\bar{1}\,0)_Y$, $[0\,\bar{1}\,1\,0]_A//[\bar{1}\,\bar{1}\,1]_Y$.[17,46,72,75,77–79]
(h) TEM Bright Field (BF) analysis of both the script and plate/rod region in the SAP-133 fiber and the script morphology of the UES fibers showed a few low angle tilt boundaries present with misfit dislocation. Most of the interphase boundaries in the as-solidified state are free of misfit dislocation. It is only after high temperature anneals that misfit dislocations form at all the interphase boundaries. This suggests that the phases are not at their equilibrium lattice parameters in the as-solidified conditions. The composition of the phases follows the undercooled (meta-stable) tie lines of the binary phase diagram. In the case of the oxide eutectic melts, that pseudo-binary phase diagram only refers to cation chemistry. The variation in oxygen content is not indicated. The non-stoichometric range for oxygen in layered and close-packed oxides are usually quite large and can significantly affect the lattice parameter. Upon annealing the chemistries adjust to equilibrium values and so do the lattice parameters. In doing so, the lattice mismatch strains are accommodated by the generation of misfit dislocations in one or both phases.
(i) TEM Dark Field (DF) analysis shows that no high angle interface boundary was present across the script to plate/rod.

4.2. Creep

Logarithmic plots of the minimum creep rate versus the applied stress at various temperatures for selected DS-AYE fibers are shown in Figs. 2a, 3a, and 4a. Note the creep data in Fig. 4a starts 100 °C higher (1500, 1600, and 1700 °C) than all the other fibers tested (1400, 1500, and 1600 °C). It is obvious from the data that the difference in microstructure scale and morphology has dramatic affected the creep behavior (as seen in the variation of the stress exponent (n) from approximately 3 to 12). This is in contrast to the bulk eutectic data where no or little threshold behavior was observed. Their the stress exponent was approximately $n = 5.0$ under all conditions tested, and the activation energy was not a function of the stress, only the temperature ($Q_{\mathrm{bulk}} = 930$ kJ/mol K). TEM micrographs from the crept samples in this fiber study showed high dislocation activity in the sapphire phase and moderate activity in the single crystal YAG phase (Fig. 5). Since dislocation were observed it is reasonable to consider a dislocation backstress argument to explain the high stress exponent observed in the logarithmic plots. One possible source for this backstress is an Orowan pile-up and bowing mechanism[80] occurring in the sapphire phase due to the presence of the more creep resistant single crystal YAG phase. The data from Figs. 2a, 3a, and 4a are replotted in Figs. 2b, 3b, and 4b by including a threshold stress that was adjusted in order to get the effective stress exponent near a value of 5 (that of the bulk eutectic data). An effective activation energy was then obtained from the slope of the log strain rate versus $1/T$ plots (Fig. 3a–c), using $Q_{\mathrm{threshold}} = (\mathrm{slope})(R)(\ln 10)$.

This procedure was carried out for all the creep data and the effective activation energies range from 841 to 1275 kJ/mol K, which compares well with the apparent activation energy determined from the bulk eutectic. In Fig. 6, the threshold stresses for all the crept fibers are plotted versus temperature. Note the threshold stress goes to zero as expected between 1500 and 1675 °C, well below the melting point. The value of the threshold stress appears to be a strong function of the microstructure, especially in the fiber that contains the plate/rod structure.

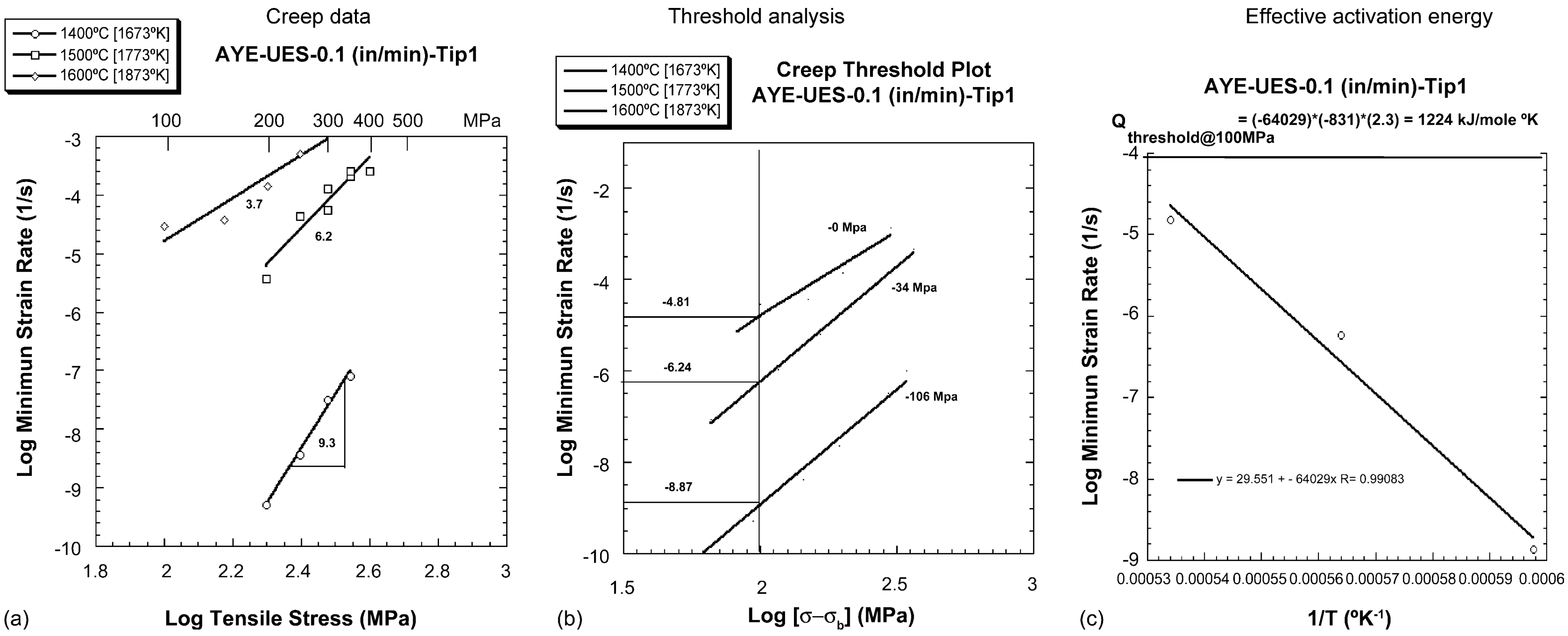

Fig. 2. Creep analysis for AYE-UES-0.1 (in./min)-tip 1 fiber.

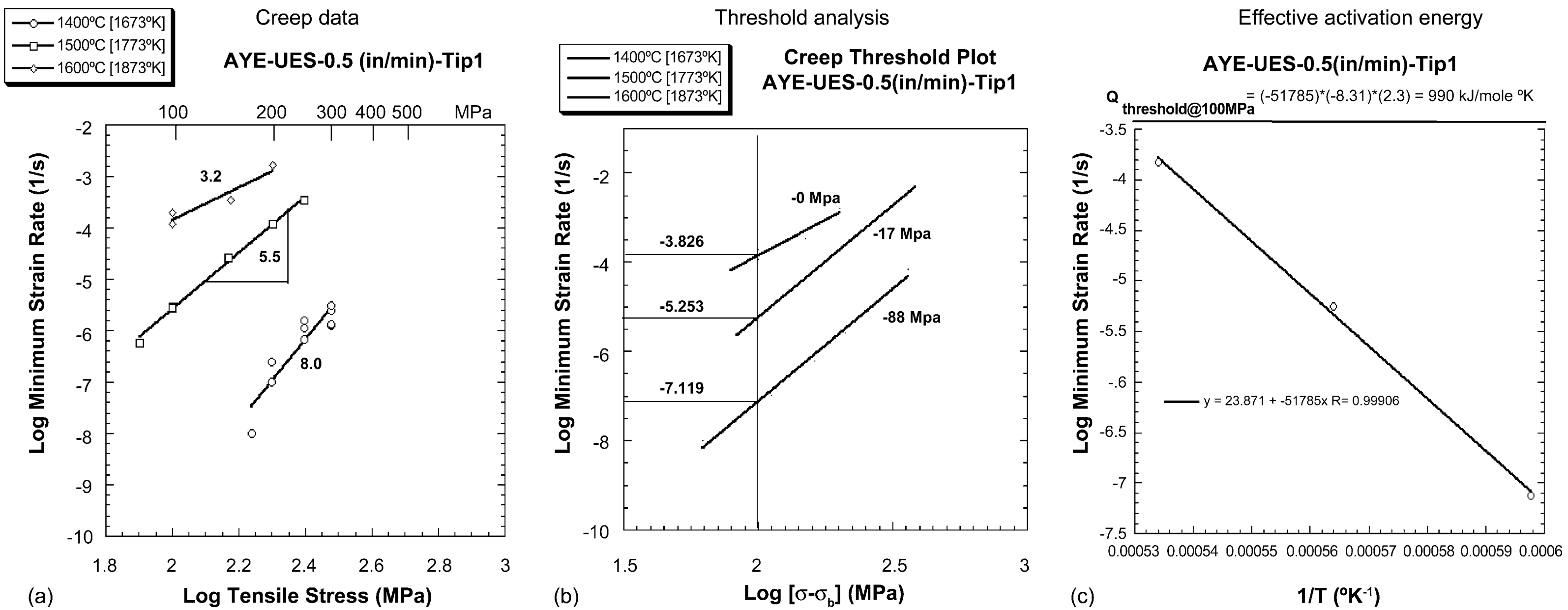

Fig. 3. Creep analysis for AYE-UES-0.5 (in./min)-tip 1 fiber.

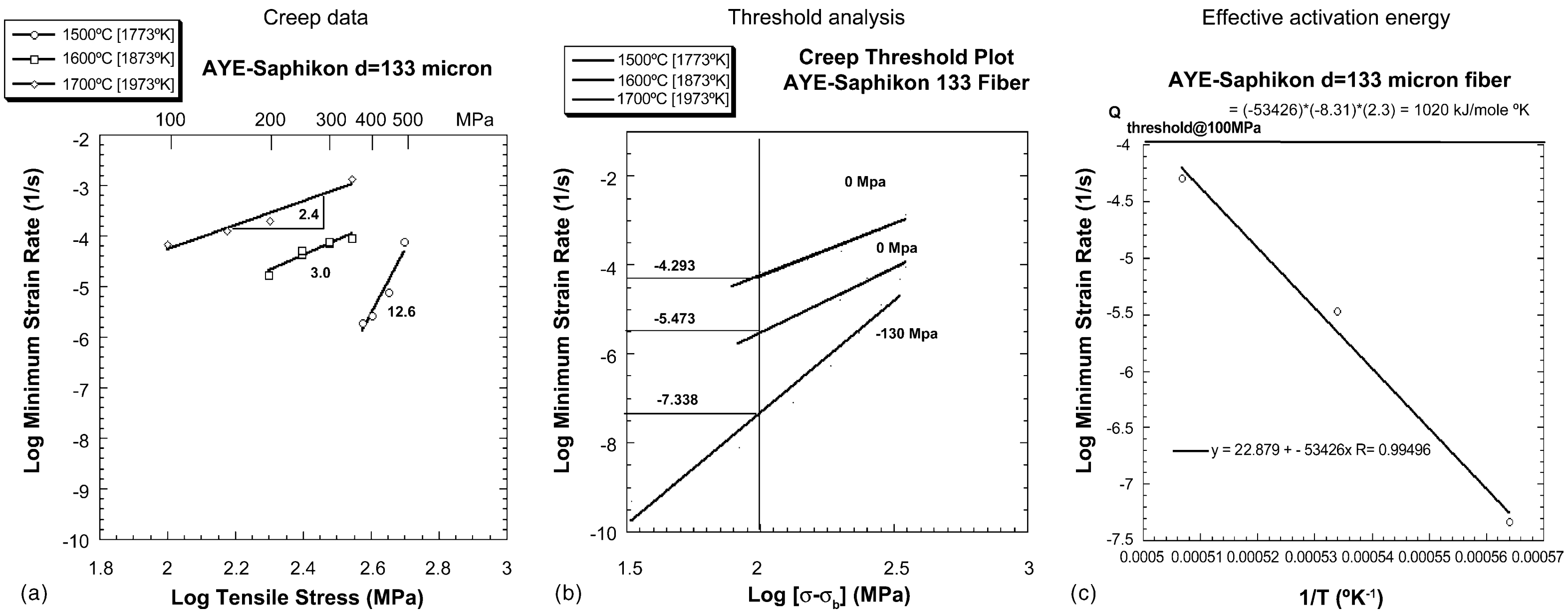

Fig. 4. Creep analysis for AYE Saphikon 133 fiber that was pulled at 1.0 in./min.

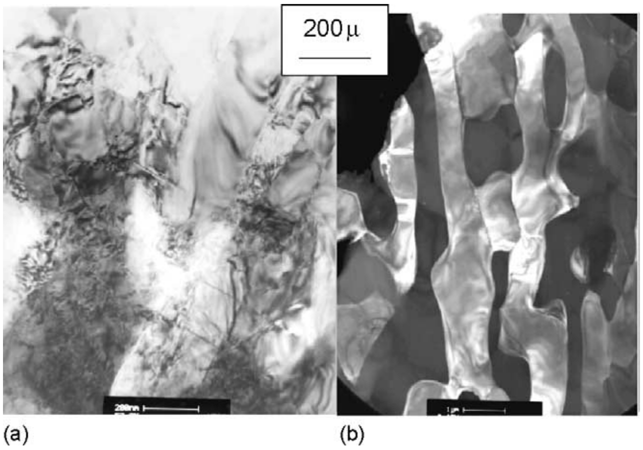

Fig. 5. TEM micrographs of AYE monofilaments crept at 1500 °C. (a) TEM bright field micrograph of AYE-SAP-133 fiber crept at 375 MPa showing high dislocation activity, shear bands, and twinning in the sapphire phase. (b) TEM dark field micrograph of AYE-UES-0.5 (in./min)-tip 1 monofilament crept at 125 MPa showing a recovered structure with dislocation networks forming low angle boundaries.

TEM observation of creep samples showed that many dislocations had been generated in the alumina phase and interacting with each other as well as piled-up at the YAG interphase boundary (Fig. 5a and b). This suggests that the dislocations are causing the generation of a far field backstress similar to that produced by the Orowan bowing mechanism observed in metallic creep. In Fig. 6 the barrier spacing for alumina that corresponds to a selected threshold stress as predicted by the Orowan bowing stress formula is calculated and plotted on the left vertical axis.

$$\sigma_{\text{threshold}} = \alpha G \frac{b}{\lambda}$$

where α is a geometrical factor taken as 0.5; G is the shear modulus of $A1_2O_3$ at 1500 °C = 110 GPa; b is the Burgers vector in A-axis $A1_2O_3 = 5.12$ Å; λ is the barrier spacing or phase spacing.

From this analysis a theoretical spacing of 4 to 6 μm would be required for the threshold stress to approach zero and provide no enhanced strengthening at 1500 °C. This behavior has been observed in the compression creep on bulk DS-AYE where the transverse phase size was greater then 6 μm and the creep stress exponent maintained a value of 5 irrespective of the temperature.[60]

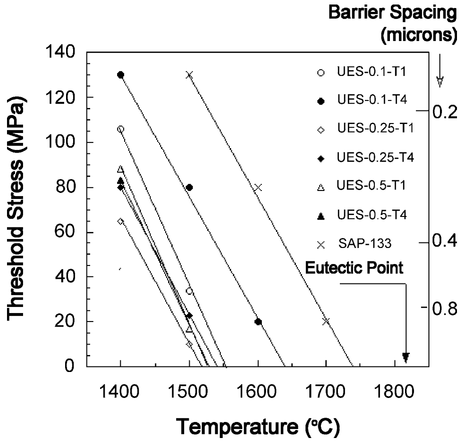

Fig. 6. Plot of the threshold stresses vs. temperature for all of the YAE fibers.

The generalized creep equation for a material can be written as follows:

$$\dot{\varepsilon}_{\text{ss}}^{\text{mech}} = A\left[\frac{G\Omega}{kTb^2}\right] D_{\text{mech}}\left[\left[\frac{b}{d}\right]^2 + \left[\frac{b}{d}\right]^3\left[\frac{D_{\text{gb}}\delta_{\text{gb}}}{D_{\text{L}}b}\right]\right]^p \times\left[\frac{\sigma}{G}\right]^n\left[\frac{P_{\text{O}_2}}{P_{\text{O}_2}^*}\right]^m \quad (1)$$

where

$$\left[\frac{G\Omega}{kTb^2} \cong \frac{Gb}{kT}\right] \quad \text{and} \quad D_{\text{mech}} = D_0 \exp\left[-\frac{Q}{RT}\right]$$

where $\dot{\varepsilon}_{\text{ss}}$ is steady state creep rate (1/s); A is a dimensionless constant containing geometrical terms of the microstructure; Ω is activation volume in terms of the burger vector b (m^3); k is the Boltzmann's constant; D_0 is a frequency factor which is temperature independent (m^2/s); D_{gb} is the grain boundary diffusion coefficient (m^2/s); D_{L} is the lattice diffusion coefficient (m^2/s); d is the grain size; m is the pressure exponent either 0 or 1; δ_{gb} is the grain boundary width; Q is the activation energy (J/mol K); R is the gas constant; $P_{\text{O}_2}^*$ is the partial pressure of O_2 in air = 0.2 atm; P_{O_2} is the partial pressure of O_2 in the testing gas (atm); D_{mech} is the diffusion coefficient for the rate limiting process such as the formation of vacancies, the migration of vacancies, ion lattice diffusion, boundary diffusion, double kink formation, dislocation core diffusion, etc. Note D_{mech} may be stoichometric dependant.

This equation reduces to the power law equation for dislocation creep in single phase-single crystal oxides crept in air atm where $m = 0$, $p = 0$, $n > 2$, $D_{\text{mech}} = D_{\text{lattice diffusion}}$

$$\dot{\varepsilon}_{\text{ss}}^{\text{mech}} \propto \rho b v = A\left[\frac{Gb}{kT}\right]\left[\frac{\sigma}{G}\right]^n D_{L_0} \exp\left[-\frac{Q_L}{RT}\right] \quad (2)$$

where ρ is the density of the mobile dislocations; b is the burger vector of the dislocation; v is the velocity of the dislocation.

In the two phase-single crystal creep where a backstress is developed, the effective stress σ is replaced with $(\sigma - \sigma_{\text{threshold}})$ and the generalized creep equation reduces to diffusion creep for fine-grained polycrystalline oxides fibers where no dislocation activity is observed. Here $m = 0$, $n = 1$, $p = 1$ and

$$D_{\text{mech}} = D_{\text{lattice diffusion and gb diffusion}}$$

$$\dot{\varepsilon}_{\text{ss}}^{\text{mech}} = A\left[\frac{Gb}{kT}\right]\left[\left[\frac{b}{d}\right]^2\left[\frac{\sigma}{G}\right] D_{L_0} \exp\left[-\frac{Q_L}{RT}\right] + A\left[\frac{Gb}{kT}\right]\left[\frac{\sigma}{G}\right]\left[\frac{b}{d}\right]^3\left[\frac{\delta_{\text{gb}}}{b}\right]\right] D_{\text{gb}_0} \exp\left[-\frac{Q_{\text{gb}}}{RT}\right] \quad (3)$$

where the first term is often refereed to as Nabarro–Herring creep and the second term Coble creep. In the complex creep case of two phase-single crystal structures, we have to impose some additional governing equations to define steady state creep.

The governing equations are as follows:

a. Strain rate continuity across the interphase boundary

$$\begin{aligned}\dot{\varepsilon}_{\mathrm{ss}}^{\mathrm{ext}} &= \dot{\varepsilon}_{\text{dislocation}}^{\text{Sapphire}} + \dot{\varepsilon}_{\text{lattice diffusion}}^{\text{Sapphire}} + \dot{\varepsilon}_{\text{ingterphase boundary diffusion}}^{\text{Sapphire}} \\ &= \dot{\varepsilon}_{\text{dislocation}}^{\text{YAG}} + \dot{\varepsilon}_{\text{lattice diffusion}}^{\text{YAG}} + \dot{\varepsilon}_{\text{interphase boundary diffusion}}^{\text{YAG}}\end{aligned} \tag{4}$$

b. Load sharing according to the volume fraction of the phases

$$\sigma_1 V_1 + \sigma_2 V_2 = \sigma_{\mathrm{ext}} \tag{5}$$

where 1 = sapphire, 2 = single crystal YAG.

c. Shape factor considerations

$$A_{\text{Diffusion}}^{\text{Lattice}} = \frac{21}{S^2}\left[\frac{(R_1R_2)^{-2/3}(R_1^2+R_2^2)}{1+R_1^2+R_2^2}\right] \tag{6}$$

where

$$S = (\mathrm{LWH})^{1/3}, \quad R_1 = \frac{L}{H}, \quad R_2 = \frac{L}{W}$$

and

$$A_{\text{Diffusion}}^{\text{Interface}} = \frac{21}{S^2}\left[\frac{((1/R_1)+(1/R^2))((R_2/R_1)+(R_1/R^2))}{(((1/R_1)+R_1+1))/(R_2+R_2 +(R_2/R_1)+(R_1/R_2))}\right] \tag{7}$$

These geometrical factors were obtained by considering the microstructure of the YAG phase in the eutectic is just the staking of rectangles, offset from each other at the out-of-plane phase facets or ledges. The factors end up being similar to factors that were originally derived by Nix[81] for Nabarro-Herring creep of polycrystalline single-phase materials with high aspect ratio grains. In this work, the following terms are defined:

R_1 is an aspect ratio of the YAG phase = L/H.
R_2 is an aspect ratio of the YAG phase = L/W.
L is the length or dimension of the YAG phase parallel to the stress axis = LCS-L.
W is the width or dimension of the YAG phase perpendicular to the stress axis = LCS-T
H is the height or dimension of the YAG phase perpendicular to the stress axis and 90° from the W dimension = TCS.

The creep geometrical factor (A) for each fiber was calculated from the as-received microstructural analysis data listed in Table 1. It was assumed that the width dimension = height dimension = TCS dimension for the YAG phase. This should be valid since the FFT ratio for all the fibers in the transverse cross-section was ~1. The length dimension was set equal to the YAG LCS-L value. Analysis of the geometrical factors alone suggests that the AYE SAP-133 monofilament should have the best creep resistance due to its low value. Followed by the AYE UES 0.1 monofilaments, which have the longest branch/facet spacing. It is important to note that this behavior is consistent with the threshold versus temperature plots of Fig. 6 and creep hypothesis.

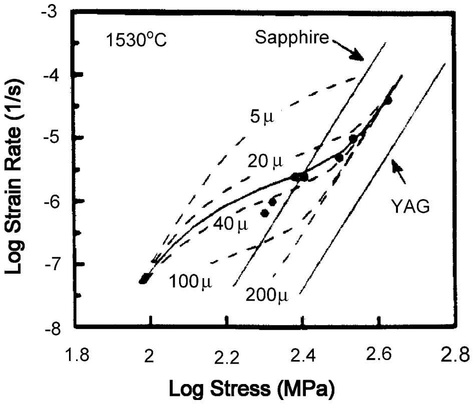

Fig. 7. Prediction by the creep model when considering the transition from lattice diffusion controlled creep in YAG to dislocation creep. The Sapphire phase is creeping by dislocation creep.

Compiling all of these equations together in order to completely describe the DS-AYE system is difficult. Some of the diffusion coefficient and activation energies are not known (i.e., especially for the interphase boundary diffusion). In the creep model proposed by Parthasarathy[13] only the following strain rate continuity conditions were used because data existed for the terms:

$$\dot{\varepsilon}_{\mathrm{ext}} = \dot{\varepsilon}_{\mathrm{DISLOCATION}}^{\mathrm{Al_2O_3}} = \dot{\varepsilon}_{\mathrm{DISLOCATION}}^{\mathrm{YAG}} = \dot{\varepsilon}_{\mathrm{DISLOCATION}}^{\mathrm{YAG}} \tag{8}$$

The prediction of this model is shown in Fig. 7 and considers the transition from lattice diffusion controlled creep in the YAG phase to dislocation controlled creep as a function of the phase length aligned along the stress axis.

It is reassuring that the threshold stress calculation, the geometrical factor calculation and the model all show the same trends. This suggest the following behavior:

a. The transverse phase spacing in the least creep resistant material ($A1_2O_3$) is important for creating the backstress by a dislocation interaction mechanisms that create a far field stress that acts on the phase boundary. The finer the transverse spacing of the eutectic, the higher the backstress created/unit strain.
b. The distance between out-of-plane facets or ledges (measured parallel to the loading axis) in the more creep resistant YAG phase is important in diffusional strain accommodation. The larger the distance between branch sites/facets the longer the diffusion path length and the higher the creep resistance. Eventually, dislocation creep must be initiated in the YAG phase or decohesion of the phase boundary must occur.

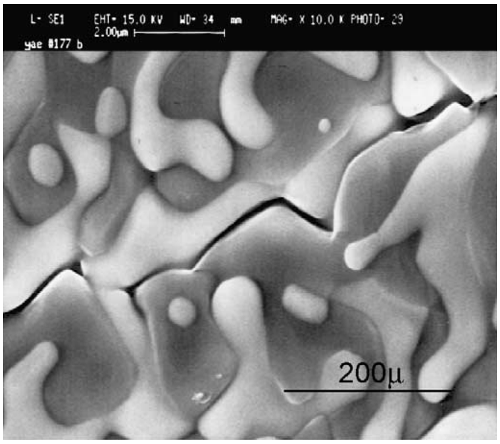

Fig. 8. SEM micrographs of an AYE-UES monofilament crept in tension at 175 MPa and 1500 °C showing rupture at the interphase boundary.

Unfortunately, the steady state creep behavior is eventually interrupted by decohesion at or near the interphase boundaries (Fig. 8). This is presumed to be related to the dislocation interactions in the alumina phase becoming sessile due to climb and not being able to move. Hence, the backstress continually increases with additional strain above the fracture stress creating cavitations at or near the interface. Rupture appeared to occur by the linkage of these decohesed boundaries into a primary crack.

5. Conclusions

The room temperature fast fracture tensile strength and the steady state creep behavior of the DS-AYE monofilaments are a strong function of microstructural scale, morphology, and distribution. *It has been shown that the finer the microstructure in the transverse cross-section the higher the tensile strength. The lower the geometrical factor is in the longitudinal cross-section the better the creep resistance. Low geometrical factors are obtained in coarses script type eutectic or fine rod eutectics*. In the UES fibers, which contain only the script type morphology, a small geometrical factor is obtained in the slowest grown fibers, which contain the coarsest microstructure, hence, the lowest strength. The creep behavior is a result of the average in-plane phase length (LCS-L) decreasing as the growth rate increased in the script morphology. This decrease is associated with the out-of-plane growth facets/branches whose density increases as the growth velocity increases. The facet ledges are areas of high tensile stress that drive diffusion relaxation at the interface boundary. When the diffusion path length is small (the out-of-plane facet density is high resulting in the in-plane length being small) then the diffusion mechanism is efficient at relaxing the backstress (that is obtained by dislocation pile-up in the alumina phase). In contrast, when the diffusion path length is large, as in the highly, aligned plate/rod structures (found in the Saphikon SAP-133 fiber), then the diffusional mechanism is not as efficient at relaxing the backstress, hence it is increased. This behavior can be seen by comparing the threshold creep data (Fig. 4b) where the Saphikon SAP-133 fiber shows about 100 °C increase in creep resistance over the much coarser microstructure found in UES-0.1-T1 fiber (Fig. 2b), even though both have low geometrical factors. Similar comparisons can be made between the coarser and finer microstructures of the UES creep data.

It has been shown that the creep mechanisms observed in these materials involves dislocations in the sapphire phase and diffusional accommodation in the YAG phase. The apparent activation energy for the creep process is high $\cong$ 1000 kJ/mol K which compares well with the bulk eutectic data. It is important to note that even the fibers with the worst creep resistance and high strength produced by UES Inc. were still 300–400 °C better than any commercial polycrystalline oxide fiber. Additionally, the creep resistance is just slightly lower than that of single crystal sapphire fibers.

References

1. Courtright, E. L., Engineering property limitations of structural ceramics and ceramic composites above 1600 °C. *Ceram. Eng. Sci. Proc.*, 1993, **12**, 1725–1744.
2. Fox, D. S. and Smialek, J. L., Burner rig hot corrosion of silicon carbide and silicon nitride. *J. Am. Ceram. Soc.*, 1995, **73**(2), 303–311.
3. Swab, J. J., U.S. Army Material Technology Laboratory, Properties of yttria-tetragonal zirconia polycrystal materials after long-term exposure to elevated temperatures. U.S. Army Material Technology Laboratory Report MTL TR 89-21, 1989.
4. Courtright, E. L., Katz, A. P., Kearns, R. J. and Graham, H., Ultra high temperature composite assessment study. AFWL-TR-91-4061, 1991.
5. DiCarlo, J. A., Hurst, J. B., Morschen, G. N., Sayir, A. and Selover, G., Current issues for SiC and oxide fiber development. HITEMP Review, NASA Conf. Pub. 10051, Cleveland, OH, 1990.
6. DiCarlo, J. A., High temperature structural fibers—status and needs. *NASA Tech. Memo.*, 1991, **105174**.
7. DiCarlo, J. A., Creep limitations of current polycrystalline ceramic fibers. *Comp. Sci. Tech.*, 1994, **51**, 213–222.
8. Wilson, D. M., Lunenburg, D. C. and Lieder, S. L., High temperature properties of Nextel 610 and alumina-based nanocomposite fibers. *Ceram. Eng. Sci. Proc.*, 1993, **14**(7/8), 609–621.
9. Wilson, D. M., Lieder, S. L. and Lueneburg, D. C., Microstructure and high temperature properties of Nextel 720 fibers. *Ceram. Eng. Sci. Proc.*, 1995, **16**(5), 1005–1014.
10. Halloran, J. W. and Laine, R. M., Creep resistant oxide fibers. USAF/WDRC #F33615-91-C-5650, 1991.
11. Halloran, J. W., Laine, R. M., King, B. H. and Liu, Y., Creep resistant oxide fibers. USAF/WL-TR-94-4100, 1994.
12. King, B. H. and Halloran, J. W., Polycrystalline yttrium aluminum garnet fibers from colloidal sols. *J. Am. Ceram. Soc.*, 1995, **78**(8), 2141–2148.
13. Parthasarathy, T. A., Mah, T. and Keller, K., Creep mechanism of polycrystalline yttrium aluminum garnet. *J. Am. Ceram. Soc.*, 1992, **75**(7), 1756–1759.
14. Corman, G. S., Creep of oxide single crystals. USAF/WRDC-TR-90-4059, 1990.
15. Corman, G. S., High temperature creep of some single crystal oxides. *Ceram. Eng. Sci. Proc.*, 1991, **12**(9/10), 1745–1767.

16. Kotchinok, D. M. and Tressler, R. E., Deformation behavior of sapphire via the prismatic slip system. *J. Am. Ceram. Soc.*, 1980, **63**(7/8), 429–437.
17. Matson, L. E., Hay, R. S., Corman, G. S., Scheltens, F. J. and Fraser, H. L., *Creep of Single Crystal Yttrium-Aluminum Garnet* (*YAG*). Presented at the 15th Annual Conference on Ceramics and Advanced ceramic Composite, Cocoa Beach, FL, 1991.
18. Collins, J. M., Bates, H. E. and Fitzgibbon, J. J., Growth and Characterization of Single Crystal YAG Fibers. Saphikon Inc., USAF/WL-TR-94-4085, 1994.
19. Corman, G. S., In *Strength and creep of single crystal YAG fiber*, 1992.
20. Corman, G., Development of single crystal YAG fibers and their properties. *SDIO Newsletter*, 1993, **10**, 11–13.
21. Sheehan, J. E., *Mechanical Properties of Single Crystal Oxide Fibers*. DOD/CIAC Workshop on Ceramic Matrix Composites, Alexandria, VA, 1991.
22. Firestone, R. F. and Heuer, A. H., Creep deformation of zero degree sapphire. *J. Am. Ceram. Soc.*, 1976, **59**(1/2), 24–29.
23. Jones, L. E. and Tressler, R., The high temperature creep behavior of oxides and oxide fibers. NASA CR-187060, 1991.
24. Sheehan, J. E., Sigalovsky, J., Haggerty, J. S. and Porter, J. R., Mechanical properties of $MgAl_2O_4$ single crystal fibers. *SDIO Newsletter*, 1993, **10**, 5–11.
25. Sheehan, J. E., Sigalovsky, J. and Haggerty, J. S., *Mechanical Properties of $MgAl_2O_4$ Single Crystals*. Presented at the 17th Annual Conference on Composites and Advanced Ceramics, Cocoa Beach, FL, January 1992.
26. Sheehan, J. E. and Haggerty, J. S., In *Single Crystal Magnesium Aluminum Spinel Fibers*. DOD/BNW Labs/MSNW Inc., 1993.
27. Sayir, A., Time dependent strength of sapphire fibers at high temperatures. In *Advances in Ceramic Matrix Composites I*, ed. N. Bansal. Am. Ceram. Soc., Westerville, OH, 1993, pp. 691–702.
28. Wiederhorn, S. M., Hockey, B. J. and Roberts, D. E., Effects of temperature on the fracture of sapphire. *Phil. Mag.*, 1973, **28**, 783–796.
29. Crane, R. L., An Investigation of the Mechanical Properties of Silicon Carbide and Sapphire Filaments. USAF/AFML-TR-72-180, 1972.
30. Crane, R. L. and Tressler, R. E., Effects of surface damage on the strength of C-axis sapphire filaments. *J. Comp. Mat.*, 1971, **5**, 537–541.
31. Pysher, D. J., Goretta, K. C., Hodder, R. S. and Tressler, R. E., Strengths of ceramic fibers at elevated temperatures. *J. Am. Ceram. Soc.*, 1989, **72**(2), 284–288.
32. Tressler, R. E. and Barber, D. J., Yielding and flow of sapphire fibers. *J. Am. Ceram. Soc.*, 1974, **57**(1), 13–19.
33. Viechnicki, D. and Schmid, F., Investigation of the eutectic point in the system Al_2O_3–$Y_3Al_5O_{12}$. *Mat. Res. Bull.*, 1969, **4**, 129–136.
34. Viechnicki, D. and Schmid, F., Eutectic solidification in the system $Al_2O_3/Y_3Al_5O_{12}$. *J. Mat. Sci.*, 1969, **4**, 84–88.
35. Viechnicki, D. and Schmid, F., Eutectic solidification in the system $Al_2O_3/Y_3Al_5O_{12}$. *J. Mat. Sci.*, 1969, **4**, 84–88.
36. Matson, L. E., Hay, R. S. and Mah, T., Stability of a sapphire-yttrium aluminum garnet composite system. *Ceram. Eng. Sci. Proc.*, 1989, **10**, 764.
37. Mah, T., Mendiratta, M. G. and Boothe, L. A., High temperature stability of refractory oxide-oxide composites. AFWAL-TR-88-4015, 1988.
38. Mah, T., Parthasarathy, T. A., Boothe, L. A., Petry, M. D. and Matson, L. E., Directionally solidification of refractory oxide ceramic eutectic composites. WRDC-TR-90-4081, 1990.
39. Mah, T., Parthasarathy, T. A. and Matson, L. E., Processing and mechanical properties of $Al_2O_3/Y_3Al_5O_{12}$ (YAG) eutectic composites. *Ceram. Eng. Sci. Proc.*, 1990, **11**(9/10), 1617–1627.
40. Mah, T., Parthasarathy, T. A., Petry, M. D. and Matson, L. E., Feasibility study of refractory oxide eutectic fiber production. USAF/WRDC Phase I SBIR #F33615-90-C-5934, 1991.
41. Mah, T., Parthasarathy, T. A., Petry, M. D. and Matson, L. E., Development of continuous refractory oxide eutectic fibers. USAF/WRDC Phase II SBIR #F33615-91-C-5655; WL-TR-94-4087, 1994.
42. Collins, J., 75 micron YAG-alumina eutectic fiber. USAF/AFOSR Phase I SBIR #F49620-95-C-0065, 1996.
43. Collins, J., Sayir, A., Yang, J. and Dravid, V. P., 75 micron YAG–alumina eutectic fiber. USAF/AFOSR Phase II SBIR #F49620-96-C-0047, 1998.
44. Sayir, A. and Matson, L. E., Directionally solidified $Al_2O_3/Y_3Al_5O_{12}$ (YAG) eutectic fibers. In *The Proceedings from 15th Conference on Metal Matrix, Carbon and Ceramic Matrix Composites*, 1991.
45. Sayir, A., Farmer, S. C. and Dickerson, P. O., Status of single crystal and directionally solidified oxide fibers. NASA LeRC Tech Brief, 1996.
46. Sayir, A. and Matson, L. E., Growth and characterization of directionally solidified $Al_2O_3/Y_3Al_5O_{12}$ (YAG) eutectic fibers. In *Proceedings of the 4th Annual HITEMP Review*, 1991.
47. Ardell, A. J., Coarsening of directionally-solidified eutectic microstructures. In *Proceedings from Computational Material Science Conference*, 1997.
48. Ardell, A. J., Isotropic fiber coarsening in unidirectionally solidified eutectic alloys. *Metall. Trans.*, 1972, **3**, 1395–1401.
49. Yang, J. M., *Homogeneous Coarsening in AYE Fibers*. Personal communication, 1996.
50. Yang, J. M., Jeng, S. M. and Chang, S., Fracture behavior of directionally solidified $Y_3Al_5O_{12}/Al_2O_3$ eutectic fiber. *J. Am. Ceram. Soc.*, 1996, **79**(5), 1218–1222.
51. Matson, L. E., Yang, J. M., Wheeler, R. and Via, D., *Coarsening in DS AYE Monofilaments*. Presented at the Am. Ceram. Soc. Meeting, Cocoa Beach, FL, 1997.
52. Sayir, A., Dickerson, R. M., Yun, H. M., Heidger, S. and Matson, L. E., *High Temperature Mechanical Properties of Directionally Solidified $Al_2O_3/Y_3Al_5O_{12}$ (YAG) Eutectic Fibers*. Presented at the HITEMP Review 1994: Advanced High Temperature Engine Materials Technology Program, NASA CP10082, 1994.
53. Farmer, S. C., Sayir, A., Dickerson, P. O. and Draper, S. L., *Microstructural Stability and Strength Retention in Directionally Solidified Al_2O_3–YAG Eutectic Fibers*. Presented at the 20th Annual Conference on Composites and Advanced Ceramics, Cocoa Beach, FL, 1995.
54. Mah, T., Parthasarathy, T. A., Petry, D. and Matson, L. E., Processing, microstructure and properties of alumina–YAG eutectic fibers. *Ceram. Eng. Sci. Proc.*, 1993, **14**(7/8), 622–638.
55. Mah, T., Parthasarathy, T. A., Petry, M. D. and Matson, L. E., Processing, microstructure and properties of Al_2O_3–$Y_3Al_5O_{12}$ (YAG) eutectic fibers. *SDIO Newsletter*, 1993, **10**, 21–23.
56. Graham, L. D. and Kraft, R. W., Coarsening of eutectic microstructures at elevated temperatures. *Trans. AIME*, 1966, **236**, 94–102.
57. Livingston, J. D. and Cahn, J. W., Discontinuous coarsening of aligned eutectic. *Acta Metall.*, 1974, **22**, 495–503.
58. Matson, L. E. and Hecht, N., Microstructural stability and mechanical properties of directionally solidified alumina/TAY eutectic monofilaments. *J. Eur. Ceram. Soc.*, 1999, **19**, 2487–2501.
59. Parthasarathy, T. A., Mah, T. and Matson, L. E., Creep behavior of an Al_2O_3–$Y_3Al_5O_{12}$ eutectic composite. *Ceram. Eng. Sci. Proc.*, 1990, **11**(9/10), 1628–1638.
60. Parthasarathy, T. A., Mah, T. and Matson, L. E., Deformation behavior of an Al_2O_3–$Y_3Al_5O_{12}$ eutectic composite in comparison with sapphire and YAG. *J. Am. Ceram. Soc.*, 1993, **76**(1), 29–32.
61. French, J. D., Zhao, J., Harmer, M. P., Chan, H. M. and Miller, G. A., Creep of duplex microstructures. *J. Am. Ceram. Soc.*, 1994, **77**(11), 2857–2865.
62. Wolfenstine, J. and Parthasarathy, T. A., Elevated temperature deformation of a fine-grained $Y_3Al_5O_{12}$–$YAlO_3$ (20 vol.%) material. *Scripta Metall. Mater.*, 1992, **26**, 1649–1653.

63. Haggerty, J. S., Wills, K. C. and Sheehan, J. E., Growth and properties of single crystal oxide fibers. *Ceram. Eng. Sci. Proc.*, 1991, **12**(9/10), 1785–1801.
64. Sigalovsky, J., Wills, K. C., Haggerty, J. S. and Sheehan, J. E., Growth characteristics, and properties of spinel single crystal fibers. *Ceram. Eng. Sci. Proc.*, 1992, **13**(78), 183–189.
65. Eylon, D., Brandon, D. G. and Rosen, A., Creep testing of alpha iron during thermal cycling. *Fatique at Elevated Temperatures*. American Society for Testing and Materials, ASTM STP 520, 1973, pp. 311–319.
66. Jackson, K. A. and Hunt, J. D., Lamellar and rod growth. *Trans. Metall. Soc.*, 1966, **236**, 1129.
67. Jackson, K. A., *Solidification*. American Society for Metals, Metals Park, OH, 1972.
68. Fidler, R. S., Croker, M. N. and Smith, R. W., The thermodynamics and morphologies of eutectics containing compound phases. *J. Cryst. Growth*, 1972, **13/14**, 739.
69. Croker, M. N., Fidler, R. S. and Smith, R. W., The characterization of eutectic structures. *Proc. R. Soc.*, 1973, **335A**, 15.
70. Croker, M. N., McParlan, M., Baragar, D. and Smith, R. W., Anomalous eutectic growth I. *J. Cryst. Growth*, 1975, **29**, 85.
71. Croker, M. N., Baragar, D. and Smith, R. W., Anomalous eutectic growth II. *J. Cryst. Growth*, 1975, **30**, 198.
72. Matson, L. E., Hay, R. and Mah, T., Characterization of alumina–YAG and alumina–YAP eutectics. *Ceram. Eng. Sci. Proc.*, 1990, **11**(9/10).
73. Caslavsky, J. L. and Viechnicki, D. J., Melting behavior and metastability of yttrium aluminum garnet (YAG) and $YAlO_3$ determined by optical differential thermal analysis. *J. Am. Ceram. Soc.*, 1980, **15**, 1709.
74. Schmid, F. and Viechnicki, D. J., Ceramic Eutectics. Army Materials and Mechanics Research Center, Watertown, Massachusetts. AMMRC-TR-72-8, 1972.
75. Schmid, F. and Viechnicki, D., Seeding and growth of large ceramic eutectic ingots. In *Proceedings of the Conference on In Situ Composites*, 1973.
76. Sayir, A. and Matson, L. E., Strength of AYE Fibers Made by LHFZ. NASA LeRC Tech Brief, 1994.
77. Hay, R. S., Orientation relationships and interfaces between low symmetry phases in the yttria–alumina system. *MRS Symp. Proc.*, 1995, **357**, 145–151.
78. Farmer, S., Matson, L., Dickerson, R. and Sayir, A., *Crystallographic Analysis in AYE Materials*. Presented at the Am. Ceram. Soc., Cocoa Beach, FL, 2000.
79. Hay, R. S. and Matson, L. E., Alumina/yttrium-aluminum garnet crystallographic orientation relationships and interphase boundaries: observations and interpretation by geometric criteria. *Acta Met.*, 1991, **39**(8), 1981–1994.
80. Hirth, J. P. and Lothe, J., *Theory of Dislocations*. Wiley & Sons, QD921.HS6, 1982.
81. Nix, W. D., The effects of grain shape on Nabarro-Herring and Coble creep processes. *Metals Forum*, 1981, **4**(1), 38–43.